Ground-based All-Sky Mid-Infrared and Visible Imagery for Purposes of Characterizing Cloud Properties

Dimitri Klebe[a,d], Ronald D. Blatherwick[b,d], Victor R. Morris[c]

[a]Denver Museum of Nature and Science
[b]University of Denver
[c]Pacific Northwest National Laboratory
[d]Solmirus Corporation

ABSTRACT

This paper describes the All Sky Infrared Visible Analyzer (ASIVA), a multi-purpose visible and infrared sky imaging and analysis instrument whose primary functionality is to provide radiometrically calibrated imagery in the mid-infrared (mid-IR) atmospheric window. This functionality enables the determination of diurnal hemispherical cloud fraction (HCF) and estimates of sky/cloud temperature from which one can derive estimates of cloud emissivity and cloud height. This paper describes the calibration methods and performance of the ASIVA instrument with particular emphasis on data products being developed for the meteorological community. Data presented here were collected during a field campaign conducted at the Atmospheric Radiation Measurement (ARM) Southern Great Plains (SGP) Climate Research Facility from May 21 to July 27, 2009. The purpose of this campaign was to determine the efficacy of IR technology in providing reliable nighttime HCF data. Significant progress has been made in the analysis of the campaign data over the past few years and the ASIVA has proven to be an excellent instrument for determining HCF as well as several other important cloud properties. The Solmirus Corporation (the producers of the ASIVA instrument) has been funded (DESC0008650) to produce a robust diurnal HCF data product utilizing ASIVA data.

1. INTRODUCTION

The mid-infrared (mid-IR) atmospheric window from 8-13 microns (µm) has long been known to hold great promise in characterizing sky conditions for the purposes of providing valuable ground-based cloud properties and atmospheric data (Shaw et al. 2005). A thermal IR imager has the distinct advantage of directly detecting emission from clouds, rather than relying on scattered light or obscured starlight, and is not hampered by the presence of the Sun or the Moon, thus providing consistent and reliable information under a wide variety of conditions. The ASIVA's primary functionality is to provide radiometrically-calibrated imagery across the entire sky in the mid-IR. Figure 1 shows the clear-sky downwelling radiance as simulated using MODTRAN (Berk et al. 1999) for a standard mid-latitude summer atmosphere pointed at the zenith for 22 mm of precipitable water vapor (PWV), typical of conditions found at the ARM SGP site. Absorption and therefore thermal emission is dominated by water vapor at wavelengths less than 8 µm, by carbon dioxide at wavelengths greater than 13
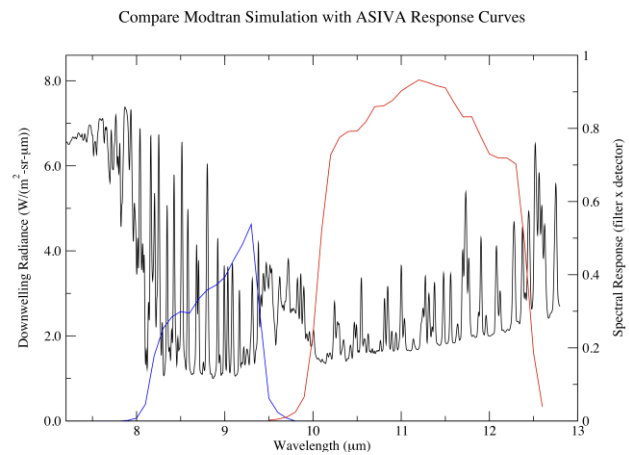
Figure 1: Simulated clear-sky downwelling radiance for 22 mm PWV pointed at the zenith. Spectral response of two ASIVA filters (red and blue) used in this research.

µm, and by ozone near 9.5 µm. Water vapor absorption lines are present throughout this spectral interval but are least prevalent in the 10.2-12.2 µm region. For this reason, a custom 10.2-12.2 µm filter for optimizing clear-sky/cloud contrast was fabricated for the ASIVA instrument. The spectral response of this filter (*shown in red*) as well the 8.25-9.25 µm filter (*shown in blue*) used in this research are presented in Figure 1.

This paper will discuss the ASIVA instrument with particular emphasis on the calibration procedures that have been developed to improve mid-IR radiometric performance. Data analysis procedures that are being developed to characterize cloud properties with particular emphasis on determining hemispherical cloud fraction (HCF) will also be discussed.

2. DESCRIPTION OF THE ASIVA INSTRUMENT

The ASIVA instrument (*shown in Figure 2*) was deployed at the ARM SGP site from May 21 to July 27, 2009. This instrument was a prototype unit that featured an infrared camera subsystem consisting of a 320×256 uncooled microbolometer array sensitive to 8-14 µm radiation, a 180-degree (all sky) custom designed hard carbon coated waterproof lens, and a filter wheel which included the two IR filters whose response is shown in Figure 1. The IR camera provided image data at 14-bit resolution and at a 30 Hz rate. Sixteen of these images were co-added to produce a single frame with an effective exposure of 0.53 seconds. Sixteen consecutive frames were then bundled to produce a 3-dimensional FITS file (data cube) that was stored to disk for future data analysis. The ASIVA visible camera subsystem featured a color progressive scan 2048x1536 CMOS detector array and a 180-degree off-the-shelf lens. The visible camera provided image data at 10-bit resolution and exposures up to 2-minutes in length. The instrument featured a unique Hatch/Radiation Shield subsystem used for radiometric calibration.


Figure 2: ASIVA at SGP Guest Instrument Facility from May 21 to July 27, 2009.

The hatch subsystem (*visible in Figure 2*) provided the following relevant features:

- Integrated the IR blackbody reference and visible dark reference into a single hatch mechanism
- IR blackbody reference and the visible reference remained in the same protected orientation (pointed downward) as the hatch mechanism was opened and closed
- Temperature sensor and a heater were embedded in the IR blackbody reference to provide in situ radiometric image calibration
- Radiation shield allowed the blackbody reference to equilibrate with the ambient air temperature

An observing script governed the data acquisition process which determined what filters and exposure times were to be used for each 5-minute data sequence. Each sequence began with the hatch closed. An IR blackbody reference image (in each of the two filters) and a visible dark reference image (of the appropriate exposure) were acquired in the closed position. The hatch was then opened wherein one visible and two infrared sky images were acquired until the next data acquisition sequence. All data sequences were identical with the exception of toggling the exposure time for the visible camera between a daytime and nighttime setting. All data were stored to disk.

A collection of images acquired on July 3, 2009 at 13:32 UTC is shown in Figure 3. An image from the ARM facility's Total Sky Imager (TSI) instrument is shown for comparison with ASIVA's visible camera. Note that the ASIVA visible image does not utilize a sun occulter and that its 10-bit resolution allows for better sensitivity near the sun. The ASIVA IR image is a single frame (0.53 second exposure) image and demonstrates that the sun's presence has almost no impact on the image.
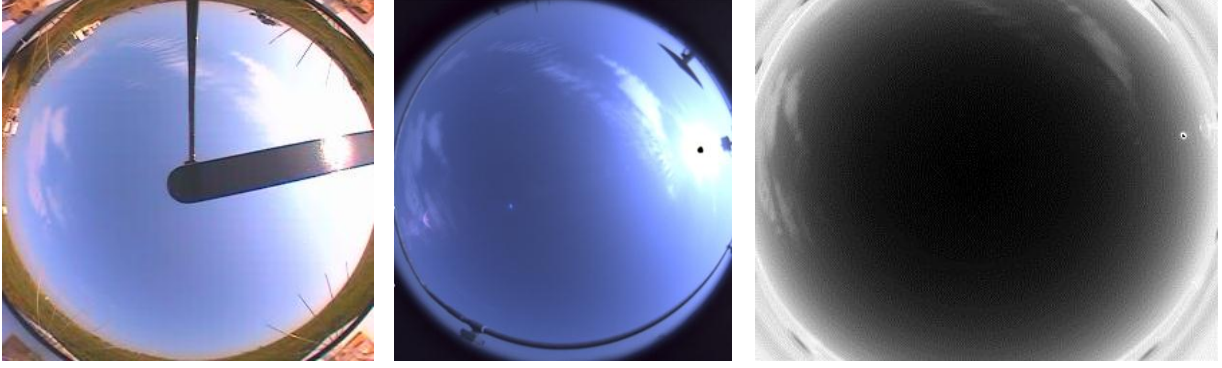
Figure 3: Three all-sky images acquired on July 3, 2009 at 13:32 UTC. a) TSI, b) ASIVA Visible, and c) ASIVA IR 10.2-12.2 µm.

3. INFRARED RADIOMETRIC CALIBRATION

3.1. Determination of Instrument Response Coefficients

A somewhat more detailed discussion of the ASIVA's calibration procedure can be found in Klebe et al. 2012. In the interest of completeness, much of that discussion is repeated here. The ASIVA instrument incorporates a two-step calibration process in determining the spectral radiance for IR images. The first step in this calibration procedure is to determine the instrument response coefficients G_λ for every pixel in the array in each IR filter. These coefficients are generated using equations (1) and (2).

$$G_\lambda = \frac{I_\lambda}{\epsilon_\lambda \cdot BB_\lambda(T)} \left\{ \frac{Counts}{Watts/m^2/\mu m/sr} \right\}, \qquad (1)$$

where I_λ = Instrumental Counts measured for the blackbody reference in a specific filter, ϵ_λ = Emissivity of the blackbody reference in a specific filter, and

$$BB_\lambda(T) = \int \frac{1.19 \times 10^8 \cdot \lambda^{-5}}{e^{1.44 \times 10^4 / \lambda T} - 1} t_\lambda d\lambda / \int t_\lambda d\lambda \, \{Watts/m^2/\mu m/sr\}, \qquad (2)$$

where t_λ = system response as a function of wavelength for a specific filter.

The blackbody spectral density equation $BB_\lambda(T)$ above assumes a wavelength λ given in units of microns (µm) and is integrated over the system response t_λ (which includes the combined effects of filter/lens transmission and nominal IR detector sensitivity as a function of wavelength) for a particular temperature T in Kelvin. The emissivity ϵ_λ of the blackbody depends on the coating and design of the calibration reference used to cover the IR lens. The emissivity is assumed to be constant for a given filter but can be adjusted from one filter to the next if necessary. A value of 0.95 was used for this study.

To eliminate instrumental offsets, G_λ was determined by calculating a least squares linear fit to the I_λ versus $\epsilon_\lambda \cdot BB_\lambda(T)$ data for a range of temperatures. The built-in blackbody reference located inside the hatch cover was used to determine the instrumental response of the system and also to measure the fixed pattern components in the image during data acquisition. A temperature sensor was bonded within the blackbody reference and the temperature data were written into the
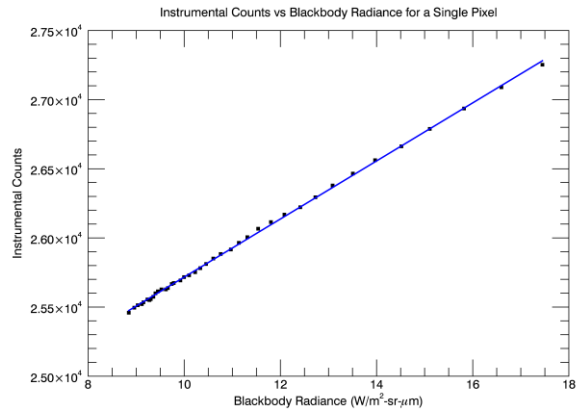
Figure 4: 10.2-12.2 µm Instrument Response for a single central pixel.

FITS header when acquiring images. A heater was embedded in the blackbody reference and was used to control its temperature during calibration.

The calibration procedure was performed on May 21, 2009. During the procedure, the hatch was opened and the blackbody was heated to ~80℃ and then allowed to passively cool down to near ambient temperature. During the cool-down period, the hatch was periodically closed (2-minute intervals) to take calibration data in each of the two IR filters. Data were acquired in this fashion for approximately sixty minutes wherein the hatch stayed open for the majority of the time to prevent heating of the IR lens during the calibration procedure. The data were analyzed as described above and a calibration image file containing the G_λ values for each pixel was created. An example of the calibration data set used to establish G_λ for a single central pixel for the 10.2-12.2 µm filter is provided in Figure 4. The response is very linear over a factor of two in radiance yielding great confidence in extrapolating to low radiance values as is done when observing clear skies with low PWV.

3.2. Calibration of Spectral Radiance Images

The sky's spectral radiance $(F_{\lambda_{Sky}})$ for a given filter is then determined using equation (3).

$$F_{\lambda_{Sky}} = \frac{I_{\lambda_{Sky}} - I_{\lambda_{Ref}}}{G_\lambda} + BB_\lambda(T_{Ref}) \ \{Watts/m^2/\mu m/sr\}, \quad\quad (3)$$

where $I_{\lambda_{Sky}}$ = Instrumental Counts measured for the sky image, $I_{\lambda_{Ref}}$ = Instrumental Counts measured for the reference blackbody image, G_λ = Instrument response coefficients derived from equation (1), and $BB_\lambda(T_{Ref})$ = Integrated Blackbody Radiance derived from equation (2) for ambient temperature T_{Ref}.

A useful quantity utilized in the analysis presented in Section 4 is the normalized spectral radiance $\mathcal{F}_{\lambda_{Sky}}$ given by equation (4). The normalized spectral radiance $\mathcal{F}_{\lambda_{Sky}}$ can be thought of as a proxy to the sky's average emissivity. $\mathcal{F}_{\lambda_{Sky}}$ is generally an underestimate of the true emissivity since the ambient temperature given by T_{Ref} is nominally greater than the mean temperature of the emitting sky.

$$\mathcal{F}_{\lambda_{Sky}} = {F_{\lambda_{Sky}}}\Big/{BB_\lambda(T_{Ref})} \quad\quad (4)$$

## 4. CLOUD DETECTION AND HEMISPHERICAL CLOUD FRACTION ANALYSIS

4.1. Verification of Calibration Procedures

The calibration procedures described in Section 3 provide the foundation for cloud detection and other cloud data products that can be derived from the ASIVA instrument. As a verification of these procedures, ASIVA spectral radiance data were compared with the precisely calibrated data retrieved from the Atmospheric Emitted Radiance Interferometer (AERI) instrument available for the campaign period. The mean spectral radiance was determined by averaging the AERI spectral radiance data over the response of each of the two ASIVA IR channels as depicted in Figure 5. The 8-minute average AERI data were utilized, as this cadence was similar to the 5-minute cadence used by the ASIVA instrument. Calibrated ASIVA data were then evaluated at the zenith, coincident with AERI's field-of-view. Comparison plots of AERI data with ASIVA data for the two daytime periods that will be highlighted in this paper are shown in Figure 6. Agreement is very good (<5%) for the two daytime comparisons and are representative of the entire campaign dataset. Note that the agreement is good in both clear and cloudy circumstances.
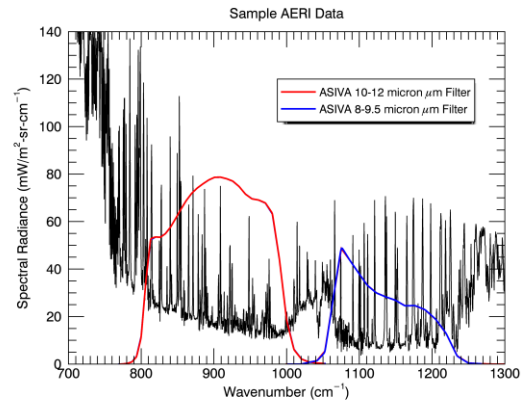
Figure 5: Sample AERI data indicating ASIVA's 10.2-12.2 µm (red line) and 8.25-9.25 µm (blue line) instrument response for which the AERI spectral radiance data were averaged.
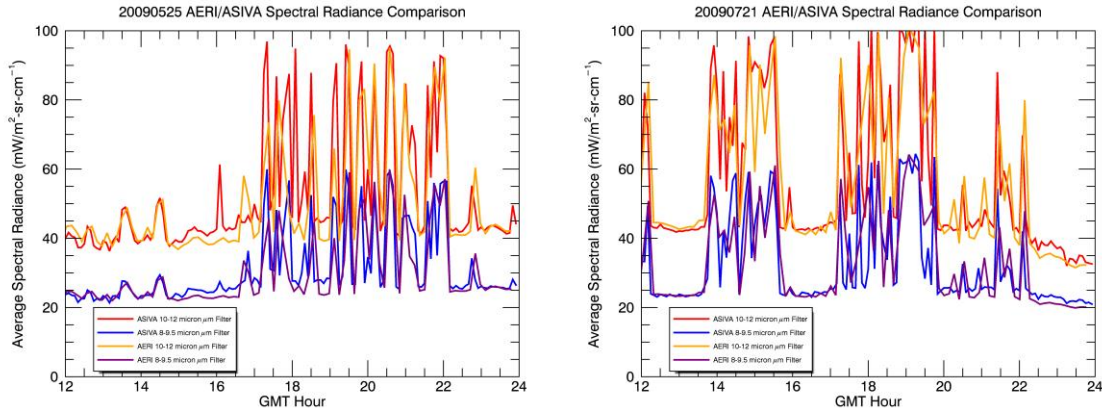
Figure 6: Comparison of AERI with ASIVA spectral radiance data in each of the two filters for May 25, 2009 (left) and July 21, 2009 (right).

4.2. Removal of Clear-sky Emission

The primary step in the cloud detection process is to remove the effects of clear-sky emission. This is done by employing the all-sky capabilities of the ASIVA instrument. Figure 7 illustrates the procedure in which the clear-sky normalized radiance is determined from the ASIVA IR image dataset. In Figure 7a, the normalized radiance pixel data are plotted as a function of airmass for the image shown in Figure 7b. The normalized radiance data are sorted into 29 airmass bins of roughly equal pixel count. The lower envelope of points in each airmass bin (*shown as red squares*) is fit to a 2nd-order polynomial equation (*gold line*) which identifies the clear-sky radiance. Even in this very cloudy image the lower envelop is still well defined (*chi-square = 0.0002*) and serves as an excellent representation of the underlying clear-sky emission. The clear-sky emission is then described as a function of airmass utilizing this polynomial equation and is then subtracted from the original normalized radiance image to yield the clear-sky subtracted image shown in Figure 7b. This image forms the basis of cloud fraction determination. A cloud/no cloud decision can be simply made by choosing a single threshold value, above which an individual pixel is determined to be cloudy. Two thresholds can be used to determine the presence of "thin" and "opaque" clouds, the criteria employed by the TSI instrument. The advantage of expressing the clear-sky subtracted image in normalized radiance is that as mentioned it is related to the emissivity of the cloud and is largely independent of ambient temperature.
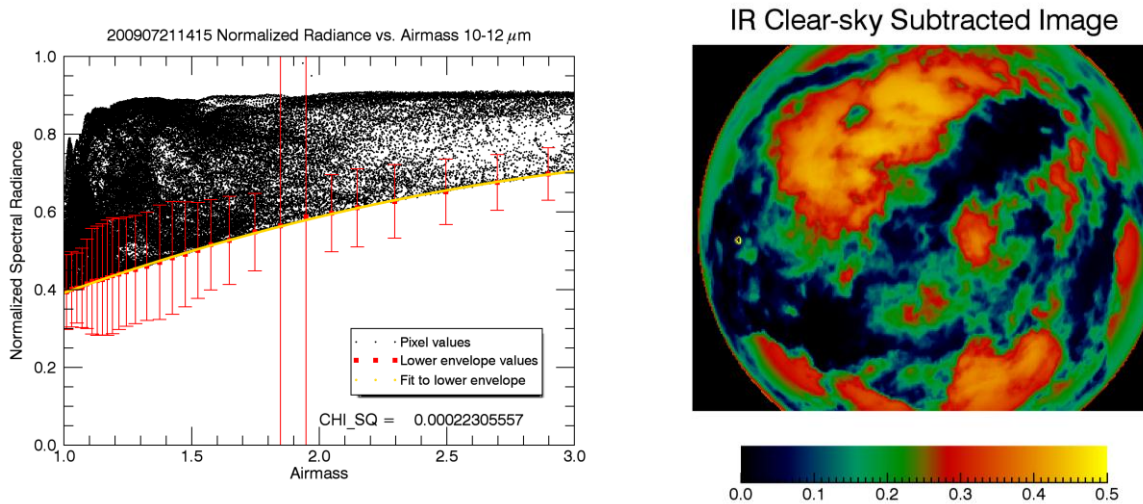
Figure 7: a) Pixel normalized radiance vs. airmass data. Gold line represents 2nd-order polynomial fit to lower envelope of points (red squares) in each of 29 airmass bins. b) Clear-sky subtracted image based on analysis shown in a). Note: Image is truncated at six airmasses. Large error bars for airmass bins near 1.9 airmass are due to the sun's extreme pixel values.

One of the primary challenges of producing a robust cloud decision map is determining the clear-sky radiance in nearly 100% cloudy conditions. This is accomplished by demanding that the chi-square value for the polynomial fit be less than some threshold (chosen to be 0.002 in this analysis) to ensure a strict goodness-of-fit criterion. If this criterion is not met, the previous polynomial equation that has met this criterion is used to define the clear-sky radiance. We have found this procedure to be very effective. A case in which the sky is nearly 100% cloudy is illustrated in Figure 8. Note that the fit denotes the proper clear-sky radiance for this image.
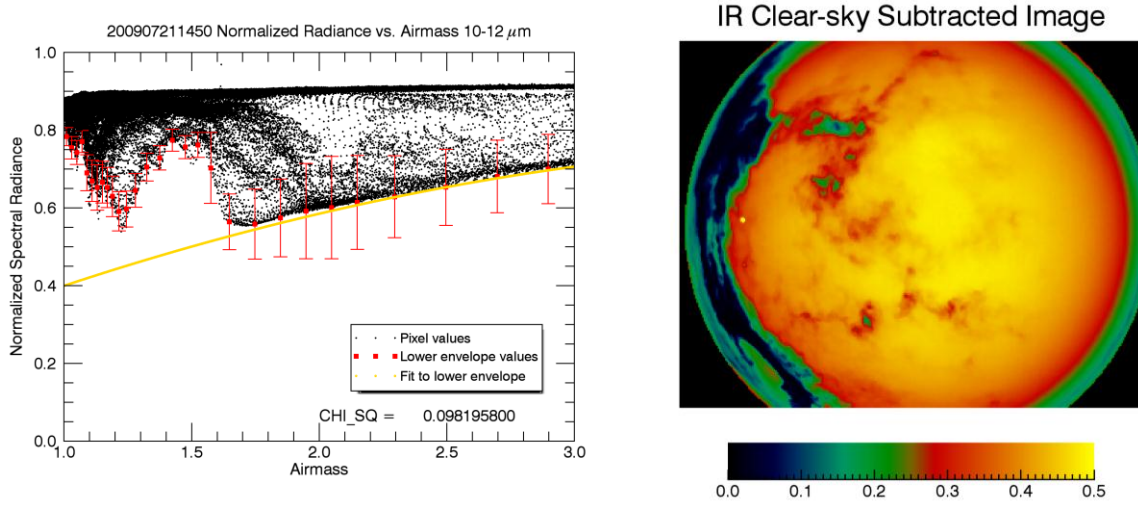
Figure 8: a) Pixel normalized radiance vs. airmass data. Gold line represents 2nd-order polynomial fit to lower envelope of points obtained from the previous dataset that met the chi-square < 0.002 criterion. b) Clear-sky subtracted image based on analysis shown in a).

### 4.3. Hemispherical Cloud Fraction Determination

After determining the clear-sky emission, cloud decision masks can be processed by applying the proper thresholds to the clear-sky subtracted images. Using the thresholds (in normalized radiance units) of 0.03 < *thin cloud* < 0.05 and *opaque cloud* ≥ .05, the HCF comparison plots derived for July 21, 2009 are shown in Figure 9.
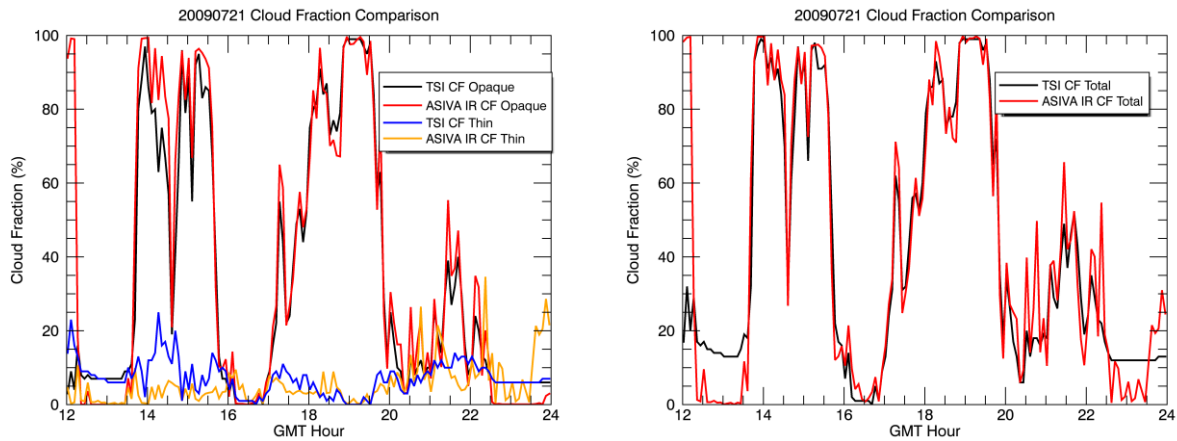
Figure 9: a) Hemispherical Cloud Fraction comparison between TSI and ASIVA IR for opaque and thin cloud types during daylight hours on July 21, 2009. b) HCF comparison between TSI and ASIVA IR for total (opaque + thin) cloud fraction.

Agreement between TSI data retrieved from the ARM archive and the ASIVA IR data for this day is excellent. Note that the TSI instrument shows erroneous cloud fraction results at the beginning and end of the day. The low sun elevation angles prove more difficult for the TSI instrument. A more sophisticated analysis package is available (Long, 2010) to improve the TSI dataset and will be used for further comparison with ASIVA data.

July 21st was dominated by thick opaque clouds. The May 25, 2009 dataset, which provided a mix of thin and opaque clouds, represents more challenging conditions for cloud fraction analysis. Figure 10 illustrates the difficulty in determining thin clouds.
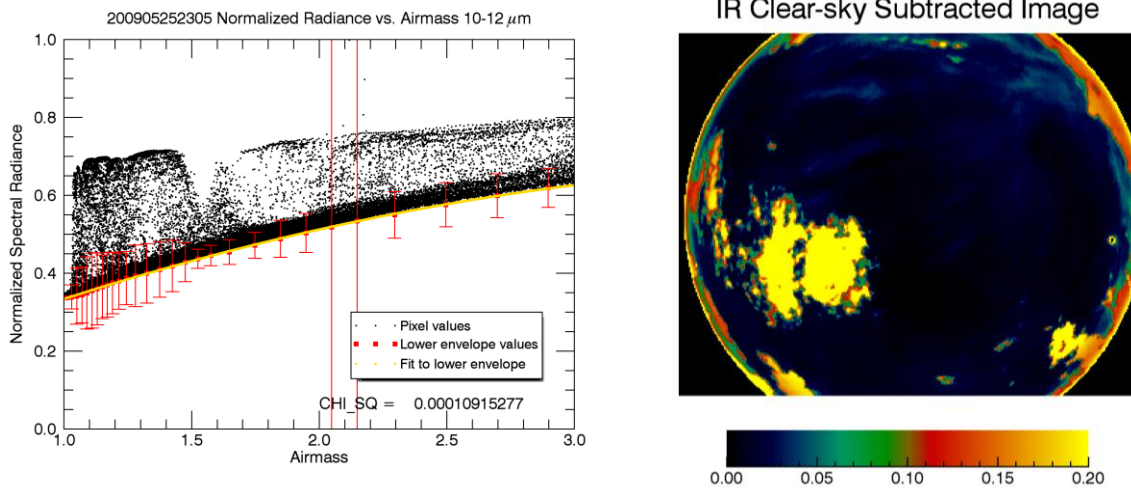
Figure 10: a) Pixel normalized radiance vs. airmass data. Gold line represents 2nd-order polynomial fit to lower envelope of points. b) Clear-sky subtracted image based on analysis shown in a).

The problem arises in that the thin cirrus clouds evident in Figure 10b (*deep blue color*) are below the thin cloud threshold of 0.03 used in the analysis of the July 21, 2009 dataset. As can be seen in Figure 11 below, much better agreement (in particular for thin cloud determination) with TSI data can be achieved by lowering this threshold to 0.016. However applying this analysis to the July 21 dataset would produce a larger fraction of thin clouds than shown in Figure 9. It may be that these thin clouds are indeed present but that the TSI is insensitive to thin clouds in highly overcast conditions. Presently we are adopting a variable lower thin cloud threshold that is dependent on opaque cloud fraction to achieve better agreement with TSI data in both of these circumstances. Basically the thin cloud threshold will be lowered in clearer sky conditions. Ultimately, we do not expect perfect agreement as the cloud decision analysis is fundamentally different between the IR and visible. However, the primary goal of this research has been to obtain as close agreement as possible between the TSI and ASIVA instrument.
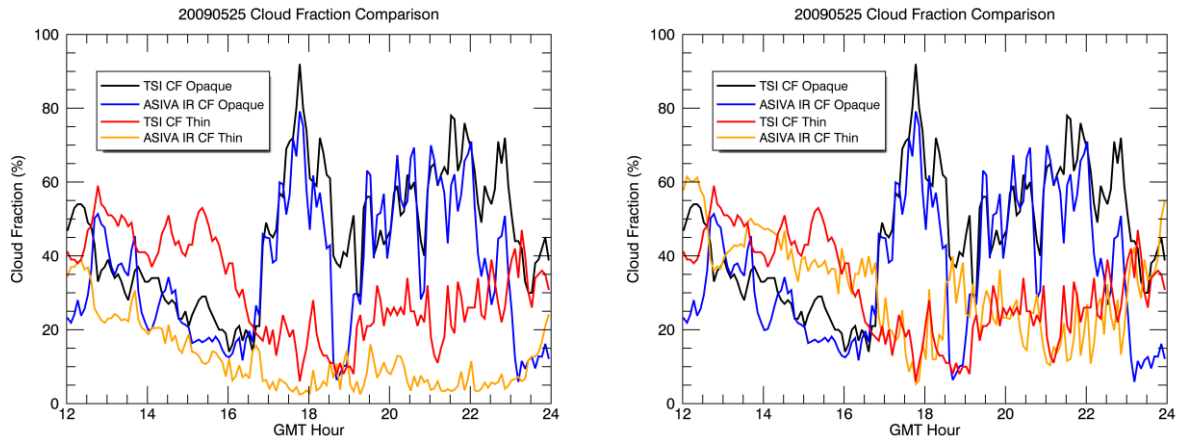
Figure 11: a) Cloud fraction comparison between TSI and ASIVA IR for thresholds 0.03 < thin cloud < 0.05 and opaque cloud ≥ .05 and b) 0.016 < thin cloud < 0.05 and opaque cloud ≥ .05.

4.4. Retrieval of HCF data product from ASIVA Visible data

Retrieval of the HCF data product from ASIVA's visible channels uses the same analysis adopted by the TSI instrument. The first-order analysis involves taking the ratio of the red image to blue image and then setting appropriate opaque/thin/no cloud thresholds (Long et al. 2006). Second-order analysis requires taking into account the Sun's position in the sky and adopting a varying threshold depending on a pixel's relative position to the Sun. Second-order analysis is easily implemented in the ASIVA instrument but was not used in the analysis presented below as it was not used in the dataset retrieved from the ARM archive. Figure 12 shows the visible red/blue ratio images coincident with the IR images shown in Figures 7 and 10. Note that the images in Figure 12 are at 90 degrees relative to those in Figures 7 and 10. The sun has been occulted in software (the larger circle) and is similar in size to the zone-of-avoidance utilized in the TSI cloud fraction analysis. In addition, a small circle is used to mask an artifact seen at the sun's position reflected through the zenith. This artifact (which can be seen in Figure 3) is brought about by internal reflection within the fisheye lens. Since the ASIVA instrument does not require a sun occulter like that utilized in the TSI instrument, eliminating this part of sky is relatively minor in the analysis.
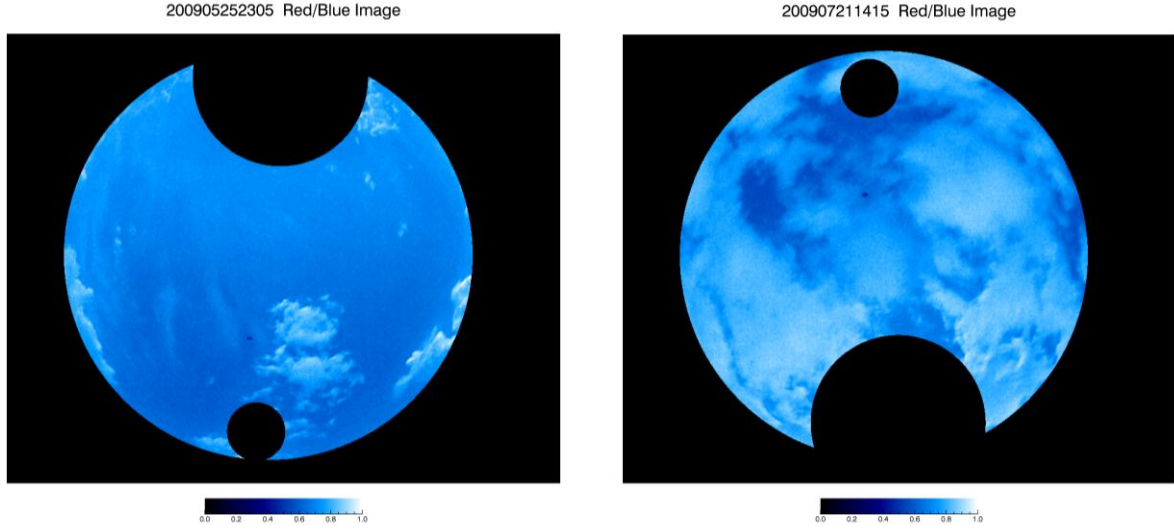
Figure 12: a) Red/Blue ratio image for May 25, 2009. b) Red/Blue ratio image for July 21, 2009.

Thresholds are then set to define the thin and opaque boundaries to provide the best agreement with the TSI instrument. Figure 13 shows the cloud fraction analysis for July 21, 2009. In contrast to the TSI, the ASIVA visible channel performs very well for low sun angles without any further processing and better matches the HCF data retrieved from the ASIVA IR channel.
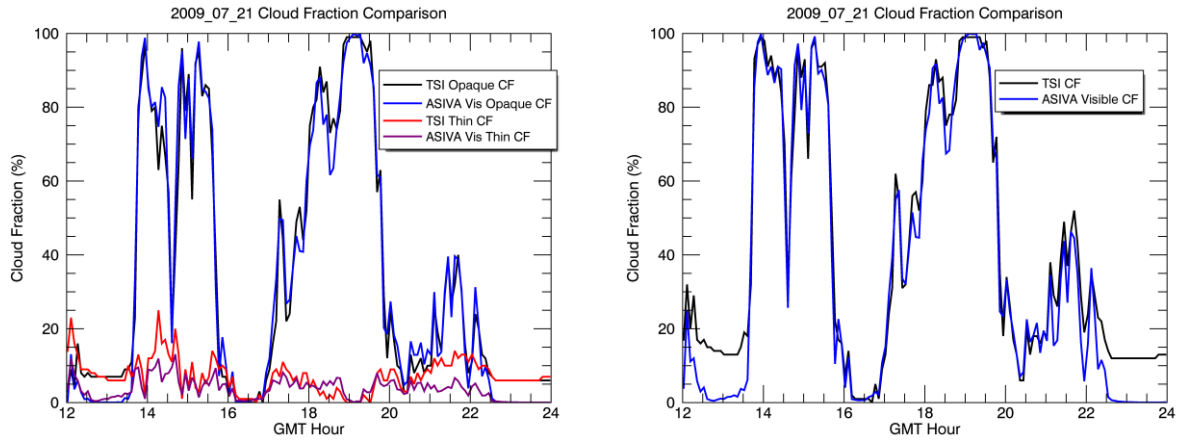
Figure 13: a) HCF comparison between TSI and ASIVA Visible for opaque and thin cloud types for July 21, 2009. b) HCF comparison between TSI and ASIVA Visible for total (opaque + thin) cloud fraction.

Using these same threshold values to determine cloud fraction for the more challenging dataset of May 25, 2009, we obtain the results shown in Figure 14. The agreement is remarkably good and demonstrates that the ASIVA visible subsystem is more than adequate reproducing TSI daytime functionality. Development of ASIVA's HCF data product is nearly complete and is currently being applied to the entire field campaign dataset.
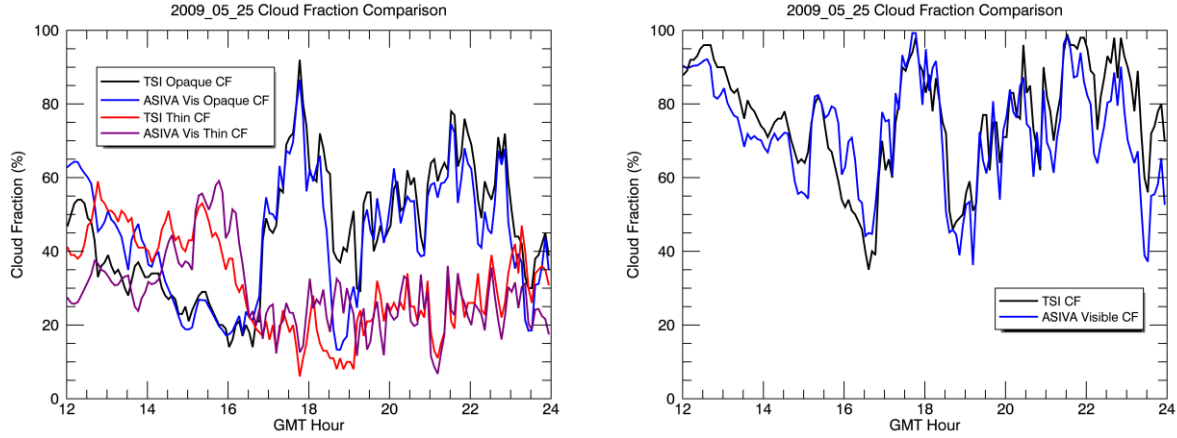

Figure 14: a) Cloud fraction comparison between TSI and ASIVA Visible for opaque and thin cloud types for May 25, 2009. b) Cloud fraction comparison between TSI and ASIVA Visible for total (opaque + thin) cloud fraction.

5. SKY/CLOUD TEMPERATURE AND OTHER POTENTIAL ASIVA DATA PRODUCTS

As a radiometrically calibrated instrument the ASIVA has the potential of delivering many other data products that will be useful to the meteorological community. This section discusses the current research in this area.

5.1. Determination of Sky/Cloud Temperature

Two temperature data products can be immediately derived from ASIVA's IR radiance data; brightness temperature and color temperature. The brightness temperature (for a given IR filter) of an image can be determined by equating the measured radiance with a blackbody whose temperature yields this same radiance. Brightness temperature images determined from the representative images of May 25th (surface temperature 304 K) and July 21st (surface temperature 297 K) are shown in Figure 15. Note that the peripheries of the clouds indicate lower brightness temperature consistent with lower optical depth in these regions.
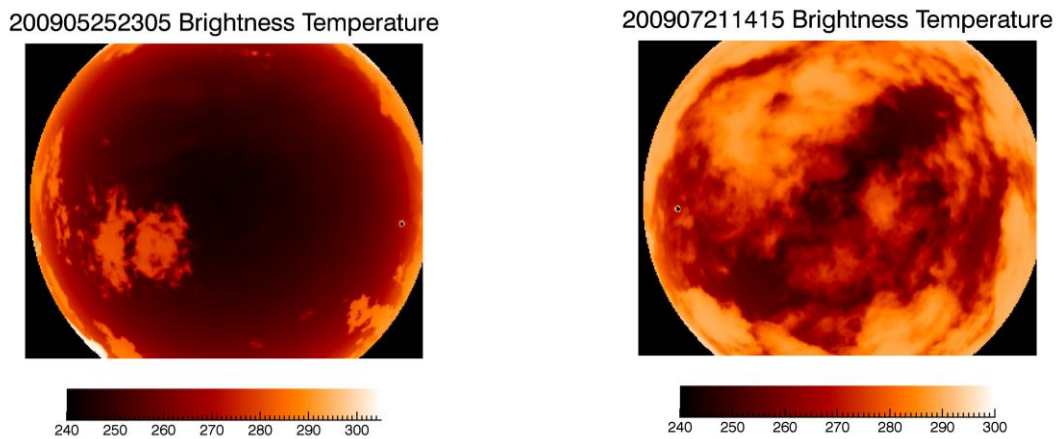
Figure 15: Brightness temperature (K) for representative images on May 25, 2009 (left) and July 21, 2009 (right).

The color temperature can be inferred by taking the ratio of sky radiance images acquired in the 8.25-9.25 μm and 10.2-12.2 μm filters and assigning this a temperature for which a blackbody yields this same radiance ratio. Color temperature has the distinct advantage of only being affected by differences in sky/cloud emissivity in the two filters but is insensitive to the total optical depth. For this reason we believe that color temperature will ultimately yield a better measure of the true temperature for optically thin clouds. Color temperature images are shown in Figure 16.
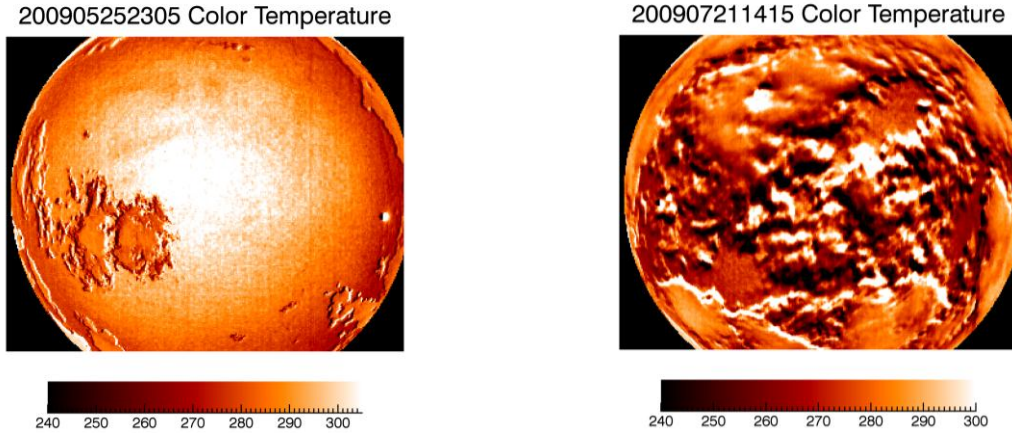

Figure 16: Color temperature (K) for representative images on May 25, 2009 (left) and July 21, 2009 (right).

Both of the images in Figure 16 show variations (both positive and negative temperature fluctuations) at the periphery of the clouds due to the motion of the clouds over the data acquisition period. This is particularly evident in the July 21st image as the clouds were very fast moving. Current ASIVA instruments now acquire 8.25-9.25 μm and 10.2-12.2 μm image data in a much shorter time interval to combat this problem. Also note that the clear-sky color temperature is higher (one would expect lower temperatures) at the zenith due to sky emissivity differences in the two IR filters. Color temperatures in the optically thick regions of clouds shown in Figure 16 are consistent with those of Figure 15 and both indicate cloud temperatures 10-20 K below the ground temperature. To some degree, these color maps already provide an estimate of cloud temperature that may be very valuable to cloud modelers. To improve on the accuracy of this measurement, one will have to account for the intervening atmospheric absorption and emission in each of the filters. This is where knowledge of PWV (discussed in Section 5.3) is required to provide additional information regarding the atmosphere's radiative properties.

5.2. Determination of Sky/Cloud Emissivity
Perhaps one of the most powerful data products that can be derived using the temperature analysis outlined above is an accurate estimate of the emissivity of an image. By assuming that the color temperature is indeed a measure of the true mean temperature for an image, one can compute a blackbody radiance image from the color temperature image. By dividing the measured radiance by the blackbody radiance derived from the color temperature, one arrives at a measure of the emissivity of the sky. Figure 17 shows the results of this analysis.
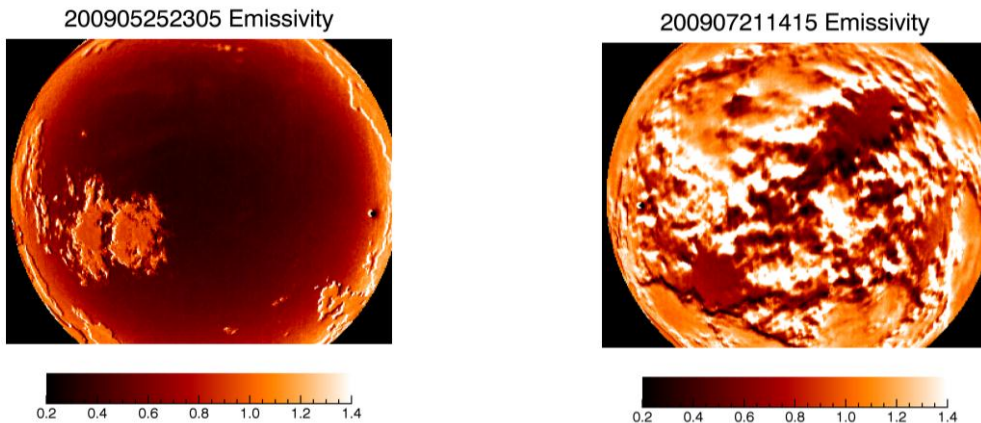

Figure 17: Emissivity images for May 25, 2009 (left) and July 21, 2009 (right).

The accuracy of this measure is somewhat hampered by the variations in emissivity between the two IR filters but can be corrected for using knowledge of the PWV burden and the information it yields regarding the atmosphere's radiative properties. Ignoring the effects of cloud motion the images of Figure 17 show cloud emissivity near unity for opaque clouds as one would expect. They also show the expected variations in clear-sky emissivity (i.e. lower emissivity at the zenith and higher emissivity near the horizon).

5.3. Determination of Precipitable Water Vapor (PWV)

As discussed above, determination of PWV is important as it can provide valuable ancillary information in the analysis of other cloud property data products, in particular refining cloud temperature measurements. The basic analysis strategy is to compare the clear-sky envelope (described in Section 4.2.) with modeled data. The model data are constructed using a series of MODTRAN simulations that provide a parameterization of the normalized clear-sky downwelling radiance as a function of PWV evaluated at different elevation angles (i.e. airmass). Preliminary simulations have been run for each of ASIVA's filters using a standard mid-latitude summer atmosphere at sea level and a lapse rate extracted from a radiosonde dataset acquired for July 21, 2009. The simulated dataset is then best fit to the clear-sky envelope determined for a particular image thus providing an estimate of PWV. Figure 18 shows the result of this analysis for the May 25, 2009 and July 21, 2009 datasets. The PWV data are compared with that retrieved from the Microwave Radiometer (MWR), an instrument with accuracy of better than 1 mm PWV. The correlation is fairly good for the July 21st dataset (the day from which the radiosonde data was used in the MODTRAN analysis) but deviates significantly for the May 25th dataset. This suggests coincidental radiosonde data may be required to improve the accuracy of ASIVA's estimate of PWV.
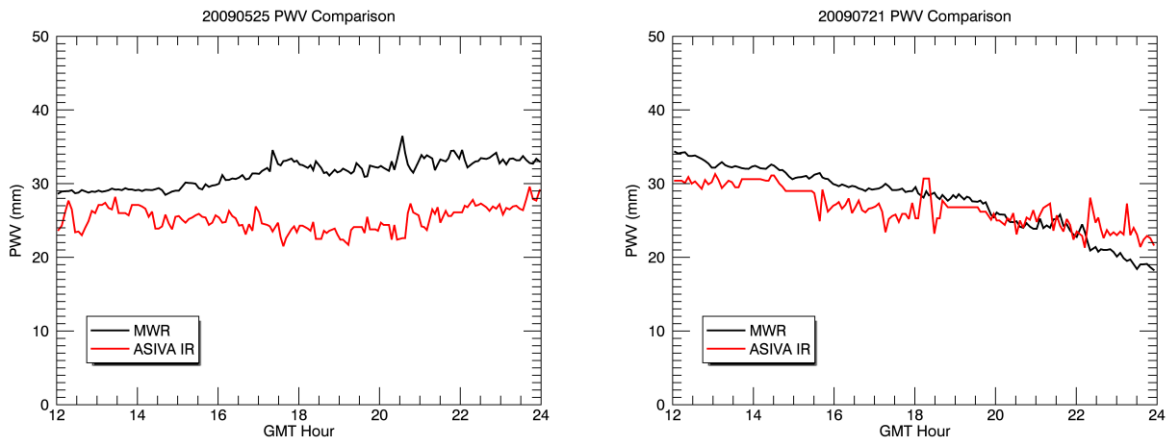

Figure 18: Comparison of MWR with ASIVA PWV data for May 25, 2009 (left) and July 21, 2009 (right).

Better accuracy in the determination of PWV may not be required in that this measure is only required to make second order corrections to data products such as the sky/cloud temperature images. If better accuracy is required, other instruments such as MWR could be used in a value added product (VAP).

5.4. Determination of Cloud Height

Cloud height can be estimated from ASIVA cloud temperature images by utilizing the altitude versus temperature information retrieved from radiosonde data. Figure 19 shows the comparison of cloud height derived from ASIVA brightness temperature images at zenith with cloud height measurements retrieved from the ARM ceilometer (CEIL) operated at SGP during the campaign period. Only very opaque clouds (*opaque cloud* ≥ .3) were used in deriving cloud height measurements in these comparisons to insure that the clouds were optically thick and that their brightness temperature was a good estimate of the cloud temperature. Agreement is good for the May 25 dataset but varies significantly for the low clouds seen in the July 21 dataset. This is presumably due to the clouds being much cooler than where the lapse rate would place them. In addition, the ASIVA instrument measures the mean temperature of the cloud to one optical depth. This will always be located at a higher altitude then the cloud base.
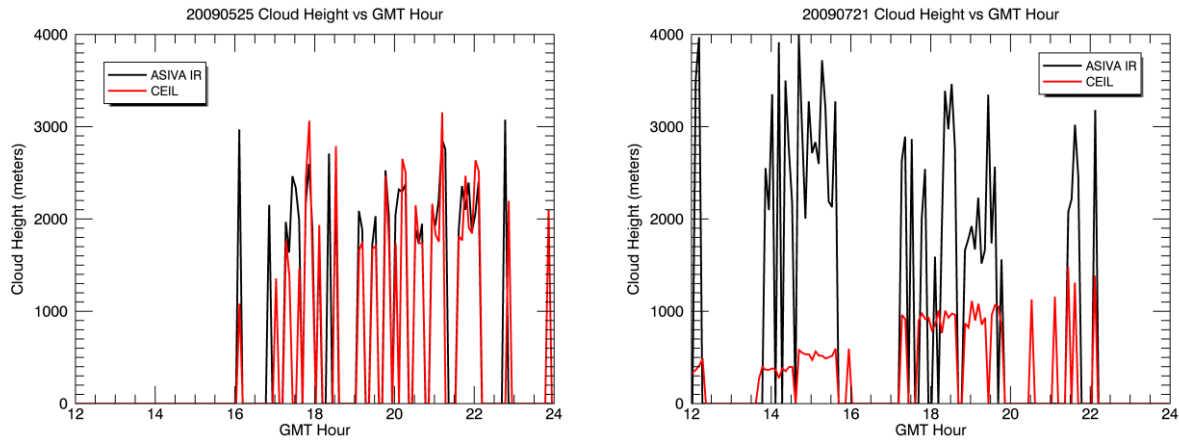
Figure 19: Comparison of cloud height derived from ASIVA brightness temperature data with ceilometer data for May 25, 2009 (left) and July 21, 2009 (right).

CONCLUSIONS

The ASIVA demonstrates considerable promise in providing a diurnal hemispherical cloud fraction data product. ASIVA HCF data (both IR and Visible) correlate very well with daytime data retrieved from the Total Sky Imager. Radiometric calibration procedures have been validated by data retrieved from the Atmospheric Emitted Radiance Interferometer. The quality of the ASIVA's radiometric data promises to yield additional products such as quality estimates of cloud temperature (both color and brightness temperature), sky/cloud emissivity, precipitable water vapor, and cloud height.

ACKNOWLEDGMENT

REFERENCES

Berk, A., G.P. Anderson, L.S. Bernstein, P.K. Acharya, H. Dothe, M.W. Matthew, S.M. Adler-Golden, J.H. Chetwynd, S.C. Richtmeier, B. Pukall, C.L. Alfred, L.S. Jeong, and M.L.Hoke, 1999: "Modtran4 radiative transfer modeling for atmospheric correction", *Optical Spectroscopic Techniques and Instrumentation for Atmospheric and Space Research III, Proceedings of SPIE Vol. 3756*, 348-353.

Klebe, Dimitri; Sebag, Jacques; Blatherwick, Ronald D.; Zimmer, Peter C.; 2012: "All-Sky Mid-Infrared Imagery to Characterize Sky Conditions and Improve Astronomical Observational Performance", *Publications of the Astronomical Society of the Pacific, 124(922)*, pp.1309-1317.

Long, C.N., J.M. Sabburg, J. Calbo, and D. Pages, 2006: "Retrieving Cloud Characteristics from Ground-Based Daytime Color All-Sky Images." *Journal of Atmospheric and Oceanic Technology 23(5)*:633-652.

Long, C.N., 2010: "Correcting for Circumsolar and Near-Horizon Errors in Sky Cover Retrievals from Sky Images", *The Open Atmospheric Science Journal*, 2010, *4*, 45-52.

Shaw, J. A., Nugent, P. W., Pust, N. J., Thurairajah, B., Mizutani, K.: "Radiometric cloud imaging with an uncooled microbolometer thermal infrared camera." *Optics Express*, 13, 5807-5817, 2005.